

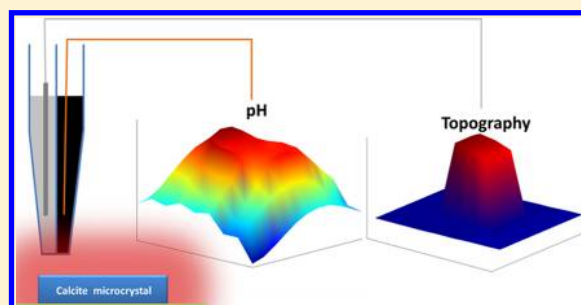
Fabrication and Characterization of Dual Function Nanoscale pH-Scanning Ion Conductance Microscopy (SICM) Probes for High Resolution pH Mapping

Binoy Paulose Nadappuram, Kim McKelvey, Rehab Al Botros, Alex W. Colburn, and Patrick R. Unwin*

Department of Chemistry, University of Warwick, Coventry CV4 7AL, U.K.

S Supporting Information

ABSTRACT: The easy fabrication and use of nanoscale dual function pH-scanning ion conductance microscopy (SICM) probes is reported. These probes incorporate an iridium oxide coated carbon electrode for pH measurement and an SICM barrel for distance control, enabling simultaneous pH and topography mapping. These pH-SICM probes were fabricated rapidly from laser pulled theta quartz pipets, with the pH electrode prepared by *in situ* carbon filling of one of the barrels by the pyrolytic decomposition of butane, followed by electrodeposition of a thin layer of hydrous iridium oxide. The other barrel was filled with an electrolyte solution and Ag/AgCl electrode as part of a conductance cell for SICM. The fabricated probes, with pH and SICM sensing elements typically on the 100 nm scale, were characterized by scanning electron microscopy, energy-dispersive X-ray spectroscopy, and various electrochemical measurements. They showed a linear super-Nernstian pH response over a range of pH (pH 2–10). The capability of the pH-SICM probe was demonstrated by detecting both pH and topographical changes during the dissolution of a calcite microcrystal in aqueous solution. This system illustrates the quantitative nature of pH-SICM imaging, because the dissolution process changes the crystal height and interfacial pH (compared to bulk), and each is sensitive to the rate. Both measurements reveal similar dissolution rates, which are in agreement with previously reported literature values measured by classical bulk methods.



The measurement of local pH is hugely valuable in explaining complex interfacial reactions, such as corrosion,^{1,2} metal deposition,^{3,4} and acid–base dissolution,^{5,6} all of which produce or consume protons and alter the pH near an interface. Additionally, many biological processes result in either intracellular^{7,8} or extracellular⁹ pH changes, and the quantitative measurement of these pH changes with high spatial resolution would aid in understanding the mechanisms involved.

While local pH can be visualized using optical techniques such as wide field fluorescence microscopy⁹ and laser scanning confocal microscopy,¹⁰ pH is commonly measured with electrodes. When deployed as the tip in scanning electrochemical microscopy (SECM), these electrodes have enabled the measurement of pH with high spatial resolution at interfaces.^{11–14} The scale on which pH electrodes can be made has advanced in recent years to the micro^{15,16} and nano scale.^{17,18}

SECM pH probes employing a variety of metal/metal oxides have been reported previously.^{15,19–21} Iridium oxide based pH ultramicroelectrodes have proven particularly popular for spatially resolved pH measurements in SECM, owing to their fast response time; long term stability over a wide range of pHs, temperatures, and pressures; all-solid format; and capability for miniaturization.^{15,22,23} Iridium oxide pH electrodes have been prepared by either electrochemical oxidation,²² thermal

decomposition,²⁴ and sputter deposition²⁵ of iridium metal or by the electrodeposition of iridium oxide from alkaline solutions of iridium salts.^{23,26} Wipf et al. used a microscopic pH electrode produced by the deposition of iridium oxide onto carbon fiber microelectrode (5.9 μm radius) to map pH changes near a platinum electrode during hydrogen evolution and for monitoring the pH change associated with the oxidation of glucose by glucose oxidase immobilized onto a carbon microelectrode.¹⁵

Hitherto, pH probes used in SECM have typically been on the several micrometers scale or larger, and consequently, constant height (conventional) SECM scanning protocols have been used (i.e., without positional feedback). For high resolution pH mapping, nanoscale probes are mandatory, and these need to be placed close to the interface of interest.²⁷ This demands the use of positional feedback SECM, particularly for samples with large topographical features.

Scanning ion conductance microscopy (SICM) has proven particularly powerful for topographical imaging of intricate surface geometries, including living cells.^{27,28} SICM uses a nanopipet filled with an electrolyte, containing a quasi-reference counter electrode, QRCE (e.g., Ag/AgCl), as the scanning

Received: June 23, 2013

Accepted: August 6, 2013

Published: August 6, 2013

probe. A potential is applied between this electrode and an external QRCE, placed in the bulk solution, and the resulting ionic conductance current provides a (feedback) signal for distance control. Various SICM-based positioning strategies have been developed over the years to expand the range of substrates open to study. Moreover, the technique has been combined with complementary techniques including SECM^{29–32} and near field scanning optical microscopy to enhance the information content.³³

Herein, we present an extremely quick and simple method to fabricate a hybrid pH-SICM probe, with an iridium oxide coated electrode for pH sensing and an SICM barrel for distance control. This report advances combined SECM-SICM²⁹ from amperometry/voltammetry to potentiometric imaging. pH-SICM probes were fabricated by the pyrolytic deposition of carbon into one of the barrels of a laser-pulled, sharp-point quartz theta pipet, followed by electrodeposition of hydrous iridium oxide to make it pH sensitive, with the open barrel forming part of the conductance cell for SICM measurement. The electrode size could be tuned by altering the pipet pulling parameters, but pH electrodes employed herein were typically on the 100 nm scale. The pH-SICM probes were employed for simultaneous mapping of pH and topography of a calcite microcrystal during dissolution to demonstrate their suitability for quantitative high spatial resolution measurements at surfaces and interfaces. This is an interesting system because the crystal size changes during dissolution, which can be traced by the topographical response, while also determining the local interfacial pH. This provides two routes to determine the dissolution kinetics, which we show are consistent. Furthermore, measurements of an entire microcrystal is topographically demanding, and hence for this study we implemented pH-SICM in both a hopping mode^{30,34} and a constant separation mode,³¹ to demonstrate the versatility of the technique.

EXPERIMENTAL SECTION

Materials and reagents and the method for the preparation of calcite microcrystals, together with instrumentation details, are available in Supporting Information (sections S1, S2 and S3, respectively).

Fabrication and Characterization of pH-SICM Probes.

The pH-SICM probes were fabricated by a two-step process. Briefly, in the first step, a quartz theta pipet (o.d. 1.2 mm, i.d. 0.90 mm, Intracel) was pulled in a laser puller (P-2000, Sutter Instruments) to a sharp point. One of the pipet barrels was closed by using 'Blu-Tack' (Bostik) and butane was passed through the other barrel, via tubing, under an argon atmosphere.²⁹ The tip of the probe was heated with a butane torch, typically for 35 s, to pyrolytically deposit carbon from the butane, as illustrated in Figure 1A, producing an extensive filling of one barrel as shown in Figure 1B. Field-emission scanning electron microscopy (FE-SEM, Supra 55-VP, Zeiss) of a typical pH-SICM probe after carbon deposition is shown in Figure 1C. A range of electrode sizes, between 40 nm and 10 μm radius (overall of the entire probe), were easily constructed by changing the laser pulling parameters during fabrication. Herein, we focus on probes with a size of ca. 100 nm across for each barrel (SECM and SICM). An electrical connection was established by inserting a copper wire through the top end of the pipet barrel to make a back contact with the carbon layer.

In the second step, electrodeposition of an iridium oxide film onto the deposited carbon layer was performed using the

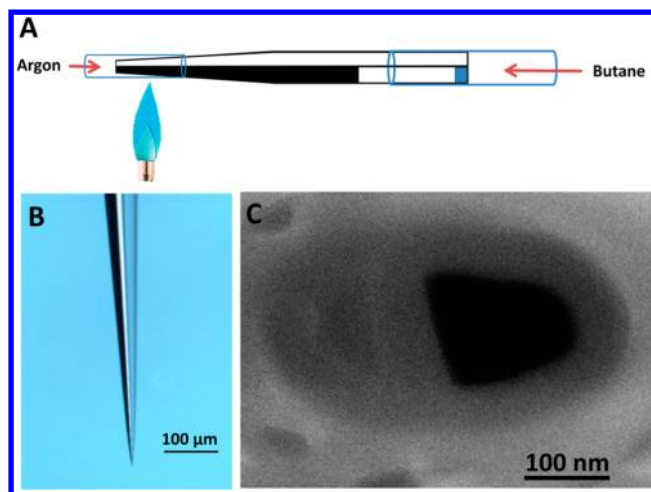


Figure 1. (A) Schematic of the carbon deposition step for the fabrication of pH-SICM probes. One barrel of a pulled theta pipet was closed using 'Blu-Tack', and butane was passed through the other open barrel and pyrolyzed using a hand-held butane torch under an argon atmosphere.²⁹ (B) Optical micrograph (side view) of a typical nanoscale pH-SICM probe after carbon deposition in one barrel. The carbon deposited barrel (left) is seen in black, along with the transparent open channel (right). (C) SEM micrograph (end view) of the tip of a typical nanoscale SICM-pH probe before electrodeposition of iridium oxide, with the carbon-filled barrel on the left and the open channel on the right.

deposition solution (see Supporting Information, section S1).^{26,35} A potential of 0.68 V versus an Ag/AgCl (0.1 M KCl) QRCE was applied for 600 s to produce a hydrated iridium oxide film (see Supporting Information, section S4). The presence of iridium oxide after electrodeposition was confirmed by energy-dispersive X-ray spectroscopy (EDX) using a Zeiss Supra55VP field emission (FE)-SEM as well as by cyclic voltammetry. The fabricated pH electrodes were initially calibrated in various pH solutions by measuring the open-circuit potential at the pH electrode versus an Ag/AgCl QRCE, using a home-built voltage follower. The home-built voltage follower incorporated a unity gain input buffer stage using an AD549L amplifier (Analog Devices Inc.) mounted on PTFE spacers to minimize leakage currents. For ultrasmall potentiometric sensors, it is important to minimize the input bias current,^{36,37} and in the measurement device we used, the input bias of the buffer stage was ca. 40 fA with an input resistance of $1 \times 10^{15} \Omega$. Stable continuous imaging over at least 3 h was achievable. To validate the calibration, the response of the pH-SICM probes was checked after each scan by titrating the solution of interest with 1 M HCl and comparing the potential response of the pH-SICM probe directly to that of a commercial glass pH electrode (Mettler Toledo International Inc.). For imaging measurements the unfilled SICM barrel was filled with 0.01 M KCl solution, and a single Ag/AgCl QRCE was inserted into it.

pH-SICM Measurement Protocol. A 350 mV bias was typically applied between the Ag/AgCl electrode inside the SICM barrel and the QRCE in the bulk solution, and a sinusoidal wave to create a 60 nm peak–peak amplitude (280 Hz) was applied to the z position of the probe. The resulting *ac* magnitude, i_{AC} , measured via the lock-in amplifier, was used to achieve close positioning of the probe to the sample and to maintain the height of the electrode from the surface as is standard in SICM;^{29,30,38} this was set on the basis of the probe

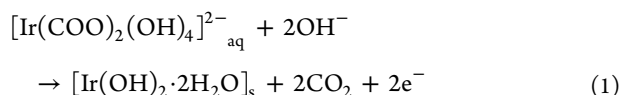
size. For the probe sizes mentioned herein, an i_{AC} of 9 pA was used as the set point for constant distance³¹ and hopping,^{29,30,34} pH-SICM imaging.

Simulations and Modeling. A three-dimensional finite element method (FEM) model, relevant to the calcite microcrystal and dissolution conditions used in the study, was developed to estimate the surface pH and dissolution rate. This mass transport model prescribed the calcite microcrystal geometry in an aqueous solution under dissolution conditions (undersaturated solution). FEM modeling was performed using Comsol Multiphysics 4.3a (Comsol AB, Sweden) using a PC equipped with an Intel core i7-3770 and 32 GB of RAM, running 64 bit Windows 7. Full details are given in Supporting Information, section S5.

RESULTS AND DISCUSSION

Fabrication and Characterization of pH-SICM Probes.

The pH-SICM probes were quickly and easily fabricated with a high success rate (80%, based on approximately 150 probes) on the day of use. The anodic electrodeposition of iridium oxide films onto the carbon nanoelectrode was achieved amperometrically using a constant-potential of 0.68 V; Supplementary Figure S1A shows a typical current–time (i – t) curve. The deposition reaction responsible for iridium oxide formation on the electrode is^{26,35}



Assuming 100% faradaic efficiency, the total amount of iridium oxide electrogenerated can be calculated by integrating the area under the i – t curve and was found to be ca. 1.3 pmol or, equivalently, 0.30 ng. Supplementary Figure S1B shows the FE-SEM image of a pH-SICM electrode after electrodeposition. No new geometrical features are observed, compared to Figure 1C, suggesting that not all of the iridium oxide electrogenerated is retained on the carbon electrode. However, retention of sufficient iridium oxide was confirmed by EDX spectroscopy; see Supplementary Figure S2. Further confirmation of the successful deposition of iridium oxide came from cyclic voltammetry (CV) of the pH probe, such as the response shown in Figure 2A, recorded between -0.4 V and 1 V in 0.5 M H_2SO_4 at a scan rate of 0.1 V s^{-1} . An anodic peak corresponding to the oxidation of Ir(III) to Ir(IV) and a cathodic peak corresponding to the reduction of Ir(IV) back to Ir(III) were observed in the CV with a similar peak potential, ca. 0.45 V on the forward and reverse waves, as reported previously,^{15,26} confirming the presence of iridium oxide. The quantity of electroactive iridium oxide on the carbon electrodes was estimated from the time integral of the cathodic peak. For the case in Figure 2A, this was ca. 0.1 pg ($8 \times 10^{-15} \text{ cm}^3$), suggesting the formation of a thin layer of iridium oxide on top of the carbon electrode.

Iridium oxide potentiometric electrodes are known to exhibit a super-Nernstian pH response, with slopes varying from -59 to -90 mV per pH unit at room temperature.²³ This has been attributed to a rather complex redox process governing the potentiometric response:^{15,26}

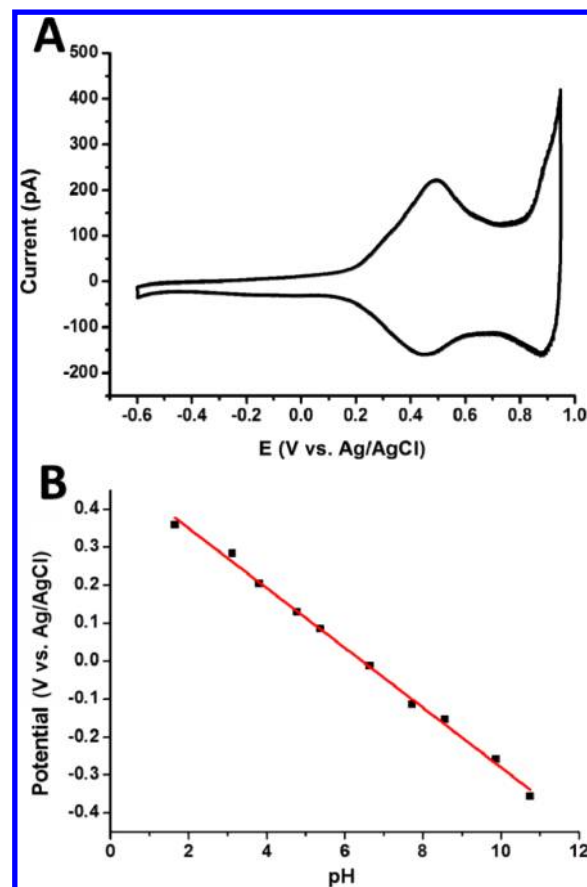
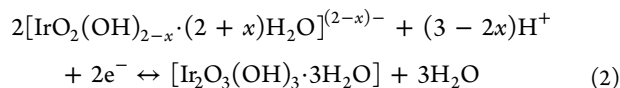


Figure 2. Characterization of the iridium oxide sensing element in a pH-SICM probe. (A) Cyclic voltammogram of the iridium oxide film after electrodeposition on the carbon electrode of a nanoscale pH-SICM probe; 0.5 M H_2SO_4 , scan rate 0.1 V s^{-1} . (B) Potential–pH calibration of a typical nanoscale pH-SICM probe.

Figure 2B shows a typical calibration curve for a nanoscale pH probe, where a slope of $79 \pm 2 \text{ mV/pH}$ was obtained over pH range 2–11, which is within the range seen with larger electrodes.^{15,23,26} This was typical of more than 70% of nanoscale electrodes that were fabricated and tested. The pH-SICM probes produced a stable response over at least 3 h of continuous imaging, but their long-term stability was not addressed in this study since probes were fabricated on the day of use.

pH Mapping of Calcite Dissolution. The dissolution of calcite is strongly pH-dependent, and this process increases the local pH at the calcite–water interface.^{39–41} The pH-SICM probe was used to map the interfacial pH and changes in crystal size that occurred during calcite microcrystal dissolution. This served to illustrate the dual capability of these probes: topography mapping combined with simultaneous local pH measurements.

For mapping of an entire calcite microcrystal during dissolution, we implemented a hopping mode similar to that reported previously for SICM.^{30,33} Thus, a series of approach curves that stopped upon reaching a specific ac set point, signifying a particular (close) distance from the surface was used to create an image. Briefly, the probe was approached to the calcite microcrystal at a speed of $0.2 \mu\text{m s}^{-1}$ while the ac component of ionic current, i_{AC} , was monitored during the approach. The pH was recorded simultaneously as a function of z -position (normal to the substrate). As soon as the value of i_{AC}

exceeded the set point, the probe was quickly withdrawn to 25 μm , moved to a new x - y pixel (in the plane of the substrate) to start a new measurement cycle. For the data reported herein, the separation between x - y pixels was 10 μm over an area of 90 $\mu\text{m} \times 90 \mu\text{m}$.

An optical micrograph of a typical calcite microcrystal, in 0.01 M KCl, obtained directly on the experimental setup, is shown in Figure 3A, and the corresponding 3-D topography

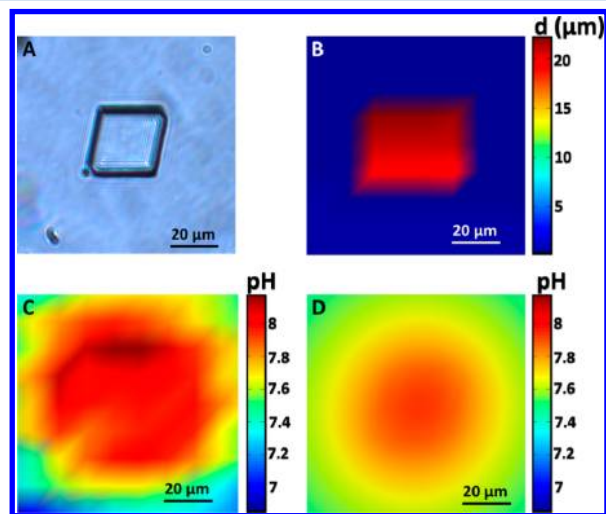


Figure 3. Topography and pH mapping of a calcite microcrystal. (A) Optical micrograph of the calcite microcrystal. (B) SICM topography image of calcite microcrystal. (C) pH map close to (100 nm from) the calcite microcrystal and glass surface recorded simultaneously with topography (bulk pH 6.85). (D) FEM model of the pH distribution close to (100 nm from) the calcite microcrystal and supporting glass substrate for a dissolution flux of $1.6 \times 10^{-9} \text{ mol cm}^{-2} \text{ s}^{-1}$.

map recorded by the pH-SICM probe is shown in Figure 3B. This SICM image is seen to match very well with the optical image, with the advantage that the SICM image provides information of the crystal height as well as the lateral dimensions. The pH map corresponding to the distance of closest approach from the surface (estimated as 100 nm, from the magnitude of i_{AC}^{38}) is shown in Figure 3C. As expected under dissolution conditions, a dramatic increase in pH was observed near the microcrystal, with the pH reaching values of ca. 7.9 ± 0.1 close to the microcrystal surface compared to a bulk value of ca. 6.85 in this particular case.

A three-dimensional FEM model, describing calcite microcrystal dissolution, was used to predict the pH on the crystal surface for different dissolution fluxes (see Supporting Information, section S5). The pH image over the calcite microcrystal and surrounding surface shown in Figure 3D corresponds to dissolution with an interfacial flux of $1.6 \times 10^{-9} \text{ mol cm}^{-2} \text{ s}^{-1}$ at the calcite/solution interface; yielding a pH 7.94, in good agreement with the surface pH recorded during the scan.

High resolution images in constant distance mode were recorded as a series of line scans over a scan area of $20 \mu\text{m} \times 20 \mu\text{m}$ with a line scan every 1 μm , each line comprising 1559 points (each the average of 512 potential measurements). The scan rate employed was $1 \mu\text{m s}^{-1}$, and the tip/crystal distance for the probe size used was ca. 100 nm, corresponding to the set-point employed.³⁶ Surface features resembling the edge of a calcite hillock^{42,43} was observed in the topographical map, demonstrating the feasibility of high resolution topography

imaging using these pH-SICM probes. To quantify the dissolution rate, two successive scans were performed on the calcite microcrystal surface, and the change in crystal height between each (Figure 4, panels A and B) was determined. The

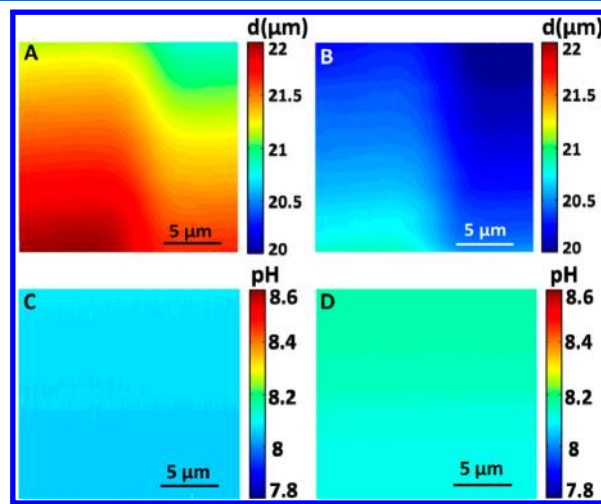


Figure 4. Simultaneous topography (A and B) and pH (C and D) images of calcite crystal surface recorded during two constant height electrochemical scans (bulk pH 6.85). Images B and D were recorded 20 min after images A and C.

two scans were performed in the same area with each of the lines in the second scan carried out 1200 s after those in the first scan. Between the two consecutive scans, an average height difference of $1.1 \pm 0.1 \mu\text{m}$ was observed (for the scanning conditions employed, the effect of thermal drift on topography measurement⁴⁴ was $<0.1 \mu\text{m}$, determined by repetitively imaging a glass surface) for an area of $400 \mu\text{m}^2$ of the crystal surface, suggesting a dissolution rate of $2.6(\pm 0.2) \times 10^{-9} \text{ mol cm}^{-2} \text{ s}^{-1}$ at pH 6.85.

Figure 4 (panels C and D) shows the respective, simultaneous pH map recorded on the surface of the calcite microcrystal. As expected the average surface pH on the calcite microcrystal surface was higher than in the bulk electrolyte, and found to be 8.05 ± 0.06 . This yields a dissolution flux of $1.9(\pm 0.2) \times 10^{-9} \text{ mol cm}^{-2} \text{ s}^{-1}$ (see Supporting Information, Figure S4 for the working curve of pH to flux), which is in good agreement with the value found above from the direct measurement of the crystal plane. Moreover, these values are in good agreement with those expected and on earlier bulk measurements.^{45,46}

CONCLUSIONS

A fast and inexpensive method to fabricate nanoscale iridium oxide based pH-SICM probes has been presented. These probes incorporate SICM-based distance feedback control and are suitable for simultaneous topography and pH imaging. The capability of these probes for generating spatially resolved pH maps of surfaces and interfaces has been demonstrated through studies of topographically challenging calcite microcrystals. Both the pH distribution and height change yield rates that are consistent with expected values based on known dissolution kinetics, highlighting the promise of these probes for high resolution quantitative pH mapping in the future.

■ ASSOCIATED CONTENT

■ Supporting Information

Materials, reagents, and the method for the preparation of calcite microcrystals, together with instrumentation details. This material is available free of charge via the Internet at <http://pubs.acs.org>.

■ AUTHOR INFORMATION

Corresponding Author

*Fax: +44 24 76524112. E-mail: p.r.unwin@warwick.ac.uk.

Notes

The authors declare no competing financial interest.

■ ACKNOWLEDGMENTS

The authors thank Dr. Neil Ebejer and Dr. Eleni Bitziou (University of Warwick), and Dr. Yasufumi Takahashi (Tohoku University) for helpful advice. We thank the European Research Council for funding (ERC-2009-AdG247143-QUANTIF) together with University of Warwick (CS studentship for B.P.N.) and EPSRC (MOAC/DTC studentship for K.M.) for additional support.

■ REFERENCES

- (1) Zhao, M. C.; Liu, M.; Song, G. L.; Atrous, A. *Corros. Sci.* **2008**, *50*, 3168–3178.
- (2) Tanabe, H.; Togashi, K.; Misawa, T.; Mudali, U. K. *J. Mater. Sci. Lett.* **1998**, *17*, 551–553.
- (3) Zhang, J. M.; Lin, C. J.; Feng, Z. D.; Tian, Z. W. *J. Electroanal. Chem.* **1998**, *452*, 235–240.
- (4) Natter, H.; Hempelmann, R. *J. Phys. Chem.* **1996**, *100*, 19525–19532.
- (5) Compton, R. G.; Unwin, P. R. *Philos. Trans. R. Soc., A* **1990**, *330*, 1–45.
- (6) Orton, R.; Unwin, P. R. *J. Chem. Soc., Faraday Trans.* **1993**, *89*, 3947–3954.
- (7) Shen, S. S.; Steinhardt, R. A. *Nature* **1978**, *272*, 253–254.
- (8) Hess, S. T.; Huang, S.; Heikal, A. A.; Webb, W. W. *Biochemistry* **2002**, *41* (3), 697–705.
- (9) Miesenböck, G.; De Angelis, D. A.; Rothman, J. E. *Nature* **1998**, *394*, 192–195.
- (10) Rudd, N. C.; Cannan, S.; Bitziou, E.; Ciani, L.; Whitworth, A. L.; Unwin, P. R. *Anal. Chem.* **2005**, *77*, 6205–6217.
- (11) Bard, A. J.; Fan, F. R. F.; Kwak, J.; Lev, O. *Anal. Chem.* **1989**, *61*, 132–138.
- (12) Bard, A. J.; Mirkin, M. V. *Scanning Electrochemical Microscopy*, 2nd ed.; CRC Press: Boca Raton, FL, 2012.
- (13) Kueng, A.; Kranz, C.; Lugstein, A.; Bertagnolli, E.; Mizaikoff, B. *Angew. Chem., Int. Ed.* **2005**, *44*, 3419–3422.
- (14) Horrocks, B. R.; Mirkin, M. V.; Pierce, D. T.; Bard, A. J.; Nagy, G.; Toth, K. *Anal. Chem.* **1993**, *65*, 1213–1224.
- (15) Wipf, D. O.; Ge, F. Y.; Spaine, T. W.; Bauer, J. E. *Anal. Chem.* **2000**, *72*, 4921–4927.
- (16) Bezbaruah, A. N.; Zhang, T. C. *Anal. Chem.* **2002**, *74*, 4428–4432.
- (17) Zhang, X.; Ogorevc, B.; Wang, J. *Anal. Chim. Acta* **2002**, *31*, 1–10.
- (18) Yamamoto, K.; Shi, G. Y.; Zhou, T. S.; Xu, F.; Zhu, M.; Liu, M.; Kato, T.; Jin, J. Y.; Jin, J. Y. *Anal. Chim. Acta* **2003**, *480*, 109–117.
- (19) Hitchman, M. L.; Ramanathan, S. *Analyst* **1988**, *113*, 35–39.
- (20) Kreider, K. G.; Tarlov, M. J.; Cline, J. P. *Sens. Actuators, B* **1995**, *28*, 167–172.
- (21) Marzouk, S. A. M.; Ufer, S.; Buck, R. P.; Johnson, T. A.; Dunlap, L. A.; Cascio, W. E. *Anal. Chem.* **1998**, *70*, 5054–5061.
- (22) Wang, M.; Yao, S.; Madou, M. *Sens. Actuators, B* **2002**, *81*, 313–315.
- (23) Elsen, H. A.; Monson, C. F.; Majda, M. *J. Electrochem. Soc.* **2009**, *156*, F1–F6.
- (24) Lodi, G.; Debattisti, A.; Bordin, G.; Deasmundis, C.; Benedetti, A. *J. Electroanal. Chem.* **1990**, *277*, 139–150.
- (25) Katsube, T.; Lauks, L.; Zemel, J. N. *Sens. Actuators* **1982**, *2*, 399–410.
- (26) Bitziou, E.; O'Hare, D.; Patel, B. A. *Anal. Chem.* **2008**, *80*, 8733–8740.
- (27) Hansma, P. K.; Drake, B.; Marti, O.; Gould, S. A.; Shiku, H.; Prater, C. B. *Science* **1989**, *243*, 641–643.
- (28) Novak, P.; Li, C.; Shevchuk, A. I.; Stepanyn, R.; Caldwell, M.; Hughes, S.; Smart, T. G.; Gorelik, J.; Ostanin, V. P.; Lab, M. J.; Moss, G. W. J.; Frolenkov, G. I.; Klenerman, D.; Korchev, Y. E. *Nat. Methods* **2009**, *6*, 279–281.
- (29) Takahashi, Y.; Shevchuk, A. I.; Novak, P.; Zhang, Y.; Ebejer, N.; Macpherson, J. V.; Unwin, P. R.; Pollard, A. J.; Roy, D.; Clifford, C. A.; Shiku, H.; Matsue, T.; Klenerman, D.; Korchev, Y. E. *Angew. Chem., Int. Ed.* **2011**, *50*, 9638–9642.
- (30) Takahashi, Y.; Shevchuk, A. I.; Novak, P.; Murakami, Y.; Shiku, H.; Korchev, Y. E.; Matsue, T. *J. Am. Chem. Soc.* **2010**, *132*, 10118–10126.
- (31) Comstock, D. J.; Elam, J. W.; Pellin, M. J.; Hersam, M. C. *Anal. Chem.* **2010**, *84*, 1270–1276.
- (32) Wei, C.; Bard, A. J. *Anal. Chem.* **1995**, *67*, 1346–1356.
- (33) Korchev, Y. E.; Raval, M.; Lab, M. J.; Gorelik, J.; Edwards, C. R. W.; Rayment, T.; Klenerman, D. *Biophys. J.* **2000**, *78*, 2675–2679.
- (34) Lazenby, R. A.; McKelvey, K.; Unwin, P. R. *Anal. Chem.* **2013**, *85*, 2937–2944.
- (35) Yamanaka, K. *Jpn. J. Appl. Phys.* **1991**, *30*, 1285–1289.
- (36) Yoon, Y. H.; Shin, T.; Shin, E. Y.; Kang, H.; Yoo, J. S.; Park, S. M. *Electrochim. Acta* **2007**, *52*, 4614–4621.
- (37) Yoon, Y. H.; Woo, D. H.; Shin, T.; Chung, T. D.; Kang, H. *J. Phys. Chem. C* **2011**, *115*, 17384–17391.
- (38) Edwards, M. A.; Williams, C. G.; Whitworth, A. L.; Unwin, P. R. *Anal. Chem.* **2009**, *81*, 4482–4492.
- (39) Stumm, W.; Morgan, J. *Aquatic Chemistry: Chemical Equilibria and Rates in Natural Waters*, 3rd ed.; John Wiley & Sons: New York, 1995.
- (40) Cravotta, C. A.; Trahan, M. K. *Appl. Geochem.* **1999**, *14*, 581–606.
- (41) Plummer, L. N.; Mackenzie, F. T. *Am. J. Sci.* **1974**, *274*, 61–83.
- (42) Kim, I. W.; Giocondi, J. L.; Orme, C.; Collino, S.; Evans, J. *Cryst. Growth Des.* **2008**, *8*, 1154–1160.
- (43) Dobson, P. S.; Bindley, L. A.; Macpherson, J. V.; Unwin, P. R. *Langmuir* **2012**, *21*, 1255–1260.
- (44) Kim, J.; Shen, M.; Nioradze, N.; Amemiya, S. *Anal. Chem.* **2012**, *84*, 3489–3492.
- (45) Rickard, D.; Sjöberg, E. L. *Am. J. Sci.* **1983**, *283*, 815–830.
- (46) Plummer, L. N.; Busenberg, E. *Geochim. Cosmochim. Acta* **1982**, *46*, 1011–1040.